Soil surface roughness modelling with the bidirectional autocorrelation function

Richard Dusséaux, Edwige Vannier

Available online at www.sciencedirect.com

ScienceDirect

journal homepage: www.elsevier.com/locate/issn/15375110

ELSEVIER

Biosystems ENGINEERING
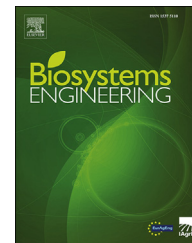
Research Paper

Soil surface roughness modelling with the bidirectional autocorrelation function

Richard Dusséaux, Edwige Vannier*

LATMOS/IPSL, Université de Versailles Saint-Quentin-en-Yvelines, 11 Boulevard d'Alembert, 78280, Guyancourt, France

Surface roughness is a major part of soil surface condition. It results from tillage operations and weathering. Surface roughness parameterisation is still a scientific lock and the object of many studies. An efficient parametrisation of soil surface roughness by modelling the bidirectional autocorrelation function estimated from 2.5D digital elevation models of soil surfaces is introduced. It not only provides geostatistical parameters that can be related to other soil surface characteristics, but let us emphasise that it reproduces the autocorrelation function with very good accuracy. The autocorrelation function is often modelled by a function of three parameters, the height variance, a single correlation length, and a roughness exponent. We added two parameters in order to take into account the anisotropy of soil surfaces and to align the coordinate system in the direction of the maximum correlation length. We propose the way to estimate roughness parameters and show its robustness for soil surfaces using laboratory tests with repeated rainfall events. One soil surface evolves from isotropy to anisotropy, and the other undergoes a reduction of initial anisotropy. The improvement brought by a second correlation length is thus highlighted. Under rainfall impact, the variation of the correlation lengths is more marked than that of the usual roughness parameter that is the root mean squared of the heights. Both parameters are complementary, capturing horizontal or vertical variation respectively. The evolution of the roughness exponent showed a slight increasing trend, which can be related to surface smoothing.

1. Introduction

Soil surface condition underlies soil-water interactions and influences hydrogeological processes such as erosion of soils by water, infiltration, water storage, runoff. Surface roughness is a major part of soil surface condition. It results from tillage operations and weathering and is an input parameter in many agronomic studies (Aguilar, Aguilar, & Negreiros, 2009; Gilliot, Vaudour, & Michelin, 2017). It is widely acknowledged that the centimetre scale is the key scale to survey soil surface roughness for understanding and modelling erosion processes (Huang & Bradford, 1992; Helming, Römkens, & Prasad, 1998; Cerdan, Souchère, Lecomte, Couturier, & Le Bissonnais, 2002; Haubrock,

---

Nomenclature

x, y, z	Coordinates in Cartesian system (in mm)
$S(x,y)$	Surface elevation at point (x,y)
1D	One dimensional
2D	Two dimensional
2.5D	Two dimensional and a half for $z(x,y)$ data
3D	three dimensional
DEM	Digital elevation model
k	State of a surface, initial and after rainfall
$S_1^{(k)}$ and $S_2^{(k)}$	Soil surfaces at state k
CCD	Charge coupled device
$m_p^{(k)}$	Spatial mean of surface p at state k
N_p	Number of samples along axes for p^{th} surface
$(x_i; y_j)$	Sampling point coordinates
Δ_p	Sampling interval
$SCI_p^{(k)}$	Chain index for surface p at state k
SSA	Specific surface area
GN	Gradient norm
$\frac{dS}{dx}$ and $\frac{dS}{dy}$	Differences in x and y directions
$MWD_p^{(k)}$	Mean weighted diameter of clods for surface p at state k
$n_p^{(k)}$	Number of clods on surface p at state k
$\mathscr{D}_i$	Equivalent diameter of clod i
s_i	Fraction of surface area covered clod i
$\mathscr{A}_i$	Area of clod i
V_i	Volume of clod i
$TV_p^{(k)}$	Total volume occupied by clods for surface p at state k
$C_p^{(k)}(x,y)$	Autocorrelation function of surface p at state k
$V_p^{(k)}$	Variance of surface p at state k
$\sigma_p^{(k)}$	Standard deviation of heights for surface p at state k
$\tilde{C}_p^{(k)}(x,y)$	Model of the autocorrelation function of surface p at state k
$(X; Y)$	Coordinates in the rotated system
$\delta_p^{(k)}$	Tilt angle between the axes OX and Ox for surface p at state k
$l_{p,X}^{(k)}$ and $l_{p,Y}^{(k)}$	Correlation lengths along the main axes OX and OY for surface p at state k
$r_p^{(k)}$	Roughness exponent of surface p at state k
$I_p^{(k)}$	Isotropy index of surface p at state k
$J_p^{(k)}$	Degree of anisotropy of surface p at state k
(x_m, y_m) and (r_m, θ_m)	Coordinates of point M in Cartesian and polar systems
$(\tilde{r}_m, \theta_m)$	Coordinates of point M on modelled ellipse in polar system
$\rho(\theta)$	Periodic function describing the modelled ellipse in polar system
$a_{p,0}^{(k)}, a_{p,1}^{(k)}$ and $b_{p,1}^{(k)}$	Coefficients of the Fourier series expansion of modelled ellipse for surface p at state k
$M_p^{(k)}$	Number of points of autocorrelation contour plot for surface p at state k
$e_{c,p}^{(k)}$	Quadratic error between autocorrelation and ellipse contour plots of surface p at state k
τ	Variable for level curves of autocorrelation function
$\bar{l}_p^{(k)}$	Average correlation length for surface p at state k
$\bar{d}_p^{(k)}(\tau)$	Average distance between points on contours and the origin
α	Intercept of linear regression
$mse_p^{(k)}$	Mean squared error of linear regression for surface p at state k
$\varepsilon_p^{(k)}(x_i, y_j)$	Error function between autocorrelations at point $(x_i; y_j)$ for surface p at state k
$\bar{\varepsilon}_{xy,p}^{(k)}$ and $\sigma_{xy,p}^{(k)}$	Mean error and standard deviation of error function for surface p at state k

---

Kuhnert, Chabrillat, Güntner, & Kaufmann, 2009; Aguilar et al., 2009; Vidal Vázquez, Rosa Vieira, Clerici De Maria, & Paz Gonzàlez, 2009; Croft, Anderson, Brazier, & Kuhn, 2013; Gilliot et al., 2017; Bullard, Ockelford, Strong, & Aubault, 2018; Vannier, Taconet, Dusséaux, & Darboux, 2018a and b; Vinci, Todisco, Vergni, & Torri, 2020) as well as for microwave remote sensing (Ogilvy, 1991; Franceschetti & Riccio, 2007; Verhoest et al., 2008). Soil surface condition is generally observed on the ground, visually and with the help of measurements, as well as remotely, by remote sensing at different frequency bands. Surface roughness parameterisation is still a scientific problem and the object of many studies, in agronomic or remote sensing fields (Atkinson & Lewis, 2000, Kamphorst et al., 2000, Vannier, Ciarletti, Gademer, 2006, Taconet & Ciarletti, 2007, Hemmat, Ahmadi, & Masoumi, 2007, Zribi, Ciarletti, Taconet, Paillé, & Boissard, 2000a, Zribi, Ciarletti, & Taconet, 2000b, Verhoest et al., 2008, Trevisani, Cavalli, & Marchi, 2009, Balaguer, Ruiz, Hermosilla, & Recio, 2010, Grohmann, Smith, & Riccomini, 2011, De Oro & Buschiazzo, 2011, Dusséaux, Vannier, Taconet, & Granet, 2012, De Keyser et al., 2012, Trevisani, Cavalli, & Marchi, 2012, Smith, 2014, Trevisani & Rocca, 2015, Martinez-Agirre, Alvarez-Mozos, & Gimenez, 2016, Moradizadeh & Saradjian, 2016, Gilliot et al., 2017, Vannier, Taconet, Dusséaux, & Darboux, 2018b, Ghorbanian, Sahebi, & Mohammadzadeh, 2019, Vinci et al., 2020). With remote sensing, the ground parameters that can be retrieved by inversion of radar data are soil roughness and moisture. This is possible to achieve by simulating the backscattered signal, which is related to these parameters, and by minimising the difference between simulated and measured radar signal (Djedouani, Afifi, & Dusséaux, 2021). The simulation of the backscattered signal can be performed by modelling the autocorrelation function of the soil surface and by applying an electromagnetic model. In some studies, empirical regressions between backscattered signals and a ground variables are derived. Unfortunately, such regressions are of limited validity and show mitigated variation of the backscattered signal as a function of the ground parameter or dispersion between related variables. In recent studies, some authors chose to circumvent uncertainties on ground roughness in order to retrieve soil parameters by combining

passive and active radar data or by developing optimization algorithms (De Keyser et al., 2012; Ghorbanian et al., 2019; Moradizadeh & Saradjian, 2016).

Among the different parameters modelling surface roughness, geostatistics has retained much attention for retrieving spatiotemporal variations in soil surface condition by ground measurements (Darboux, Davy, Gascuel-Odoux, & Huang, 2002; Friedrich et al., 2006; Anderson & Kuhn, 2008; Blaes & Defourny, 2008; Vidal Vázquez et al., 2009; Haubrock et al., 2009; Garcia Moreno, Diaz Alvarez, SaaRequejo, ValenciaDelfa, & Tarquis, 2010; Dalla Rosa, Cooper, Darboux, & Medeiros, 2012; Croft et al., 2013; Vannier, Taconet, Dusséaux, & Chimi-Chiadjeu, 2014; Bullard et al., 2018) or by remote measurements (Woodcock, Strahler, & Jupp, 1988; Atkinson & Lewis, 2000; Trevisani et al., 2009; Balaguer et al., 2010; Grohmann et al., 2011; Trevisani et al., 2012; Trevisani & Rocca, 2015). Characterising ground truth of soil surface condition is necessary for agronomic studies and for interpreting radar data. The importance of a precise localisation of microrelief structuring objects, such as mounds and depressions has encouraged the development of segmentation methods for clod delineation on 2.5D digital elevation models (DEMs) (Vannier, Ciarletti, & Darboux, 2009; Taconet, Vannier, & Le Hégarat-Mascle, 2010; Chimi-Chiadjeu, Vannier, Dusséaux, Le Hégarat-Mascle, & Taconet, 2013a; Chimi-Chiadjeu, Vannier, Dusséaux, Taconet, 2014; Vannier, Dusséaux, Taconet, & Darboux, 2019) or 2D images (Azizi et al., 2020). The autocorrelation function modelling provides geostatical parameters that are height variance, correlation length and roughness exponent (Ogilvy, 1991; Franceschetti & Riccio, 2007). Even if some local information seems to be lost with a global statistical characterisation (Chimi-Chiadjeu, Vannier, Dusséaux, & Taconet, 2013b), a modelling function of surface roughness has some advantages for further modelling, for example remote soil survey. Indeed, the accuracy of soil parameters retrieved from optical or microwave remote sensing will be dependent on the autocorrelation function shape (Zhixiong, Nan, Perdrok, & Hoogmoed, 2005; Zheng et al., 2019; Zribi, Gorrab, & Baghdadi, 2014). In these papers, the autocorrelation function was estimated from 1D soil profiles. It was therefore a mono-directional function. These works are interesting and allowed relevant information on soil surfaces to be extracted. Another approach, also currently used, relies on variograms. For instance, a set of parameters extracted from experimental semi-variograms is presented in [Balager et al., 2010] and allows a land classification of high resolution images. In this study, we introduce a new parametrisation of the bidirectional autocorrelation function estimated on 2.5 DEMs of soil surfaces. In Dusséaux et al. (2012) the bidirectional autocorrelation function was modelled by a function of three parameters, as described above, height variance, a single correlation length, and a roughness exponent. The use of a single correlation length implies that the soil surface is isotropic, which is not always the case. Therefore, in Zhixiong et al. (2005) the measurement of soil profiles was made in three directions. In the following, the model of the autocorrelation function has five parameters: root-mean-square (rms) height, two correlation lengths along two main axes OX and OY, the tilt angle between the Ox Cartesian axis and the main axis OX and the roughness exponent.

Friedrich et al. (2006) modelled a horizontal section of the bidirectional autocorrelation when modelling laboratory sand waves, and successfully captured the direction of the bed forms. The variogram approach has also shown ability to capture the anisotropy degree and direction of a soil surface in remote sensed images. The anisotropy of surface morphology is often defined by the relationship between spatial continuity to the lag distance in the direction considered and it has been studied by means of anisotropy indices derived from this relationship. In Trevisani et al. (2012) and Trevisani et al. (2015), a robust description of the anisotropy in surface spatial variability was proposed. The anisotropy of soil surface is studied here from the ratio of the minimum and maximum correlation lengths. It should be emphasised that in this study, a model of the full bidirectional autocorrelation function is proposed. To our best knowledge, this is the first time that such a model with five parameters has been applied to characterise the bidirectional autocorrelation function of soil surfaces.

2. Material and methods

2.1. Soil surfaces under study

2.1.1. Presentation of the database

The database used in the present study is composed of two laboratory made soil surfaces, which were subjected to several rainfalls in order to get a variety of roughness conditions. As shown in Table 1, a set of five successive rainfalls of two intensities and different durations was carried out. We note $S_1^{(k)}$ and $S_2^{(k)}$ the different stages of these two soil surfaces with $0 \leq k \leq 5$. Figure 1 shows a top view of some of these stages. The views at the top left and top right show the initial state $S_1^{(0)}$ and $S_2^{(0)}$ of these soil surface trays. The images on the middle represent the two soil surfaces $S_1^{(1)}$ and $S_2^{(1)}$ after the first rain and the images on the bottom line represent them after the last rain. Figure 2 shows a 3D view of one of these surfaces. To each pair of coordinates (x, y) corresponds a single and unique elevation z. Consequently, these surfaces $S(x, y) = z(x, y)$ are 2.5D DEMs (Burrough, McDonnel, & Lloyd, 1998).

To make the soil surfaces, two trays of 500×500 mm with a depth of 100 mm were used. Each tray had a permeable bottom to allow for water percolation and it was also set at a 5% slope for water runoff. Both trays were prepared with a silt loam soil composed of 11% of clay, 60% of silt and 29% of sand, and an organic matter content of 2%. Initial soil moisture was 2.4% of the total soil mass. Using a hand scoop, the trays were filled with loose soil, creating a structure similar to a seedbed.

Table 1 − Characteristics of rainfall simulations.

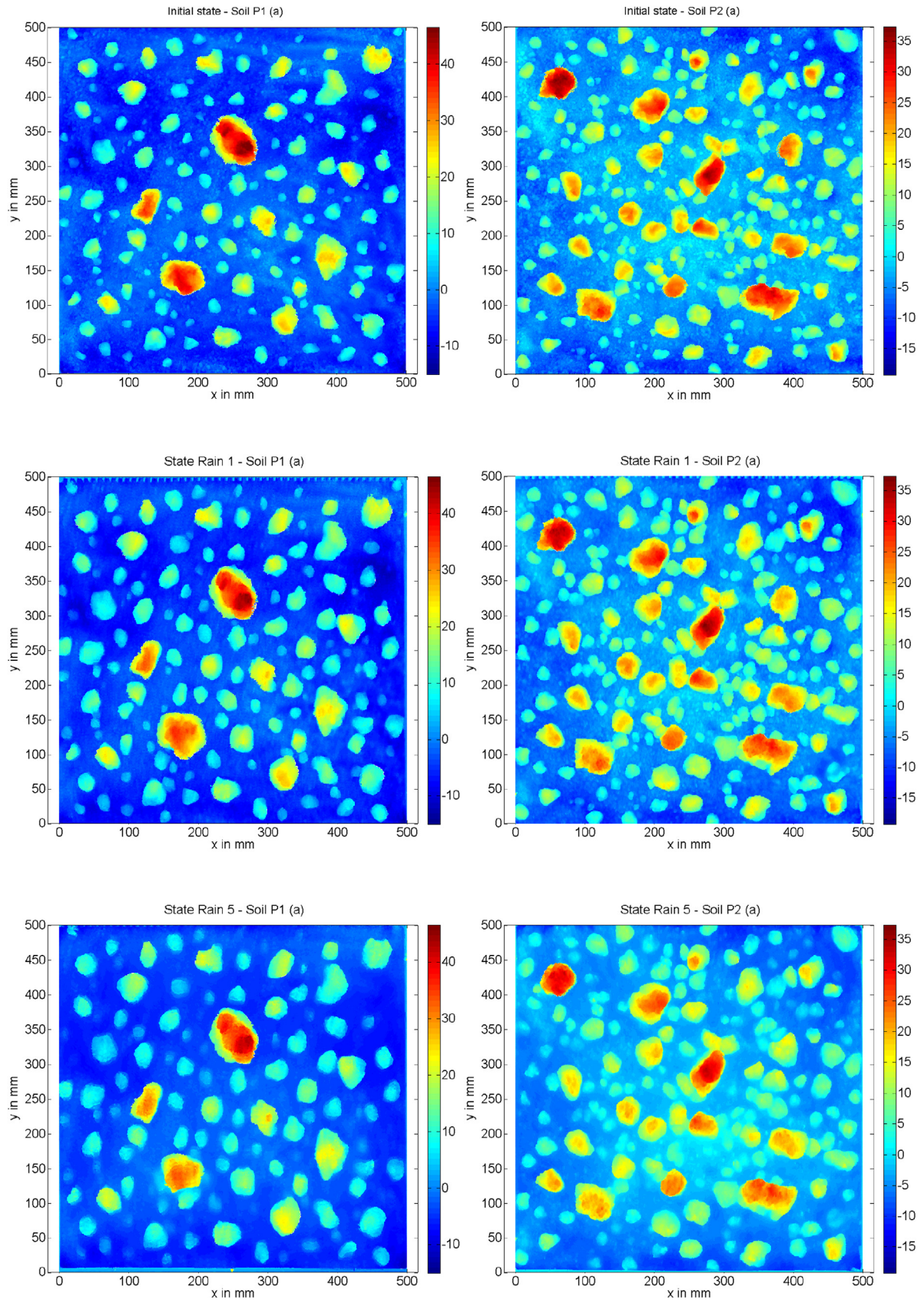| Rainfall	Intensity (mm.h^{-1})	Duration (min)	Cumulated rainfall (mm)
n°1	33	60	33
n°2	33	60	66
n°3	42	38	93
n°4	42	51	129
n°5	42	90	192

Fig. 1 — Top view of soil surfaces under study at initial state (top row), after first rainfall (middle row), after last rainfall (bottom row). Laboratory made soil surfaces with a low clod concentration (left column) and, with a high clod concentration (right column).

Air-dried clods of various sizes were set upon the soil surfaces. On each tray, a different clod concentration was used: the tray $S_1^{(0)}$ had a low clod concentration of 530 m^{-2} (see top left image of Fig. 1) and the tray $S_2^{(0)}$ had a high clod concentration of 805 m^{-2} (see image at top right of Fig. 1). There is no crusting of the plots from the start of the experiment but later on.

Soil surface evolution under successive rainfalls was performed with a laboratory rainfall simulator similar to the one described in Foster, Eppert, and Meyer (1979). As shown in Table 1, two rainfall intensities of 33 mm h^{-1} and 42 mm h^{-1} were used in order to get visually different surface conditions. The soil surfaces showed smoothing, sealing and crusting. Therefore, levelling of clods until disappearance of the smallest of them was observed. On the high clod concentration tray, the close inter-proximity of the clods induced coalescence and formation of blocks as shown in Vannier et al. (2018a) and the evolution of clods is more complex on this tray. For each stage, the soil surface elevations were recorded with an instantaneous-profile laser scanner at a grid spacing of 0.5 mm in x and y, and of 0.1 mm in z. The laser scanner used in the measurements is described in Darboux and Huang (2003). In summary, the principle of recording relies on a laser producing a line on the soil surface and a CCD camera set at an angle to measure the surface geometry along a profile in the y− z planes. The laser-camera assembly was moved automatically along a rail (x-axis), to get the whole surface geometry. With rough surfaces, such as those of the study, there were about 20% of missing data points due to shadowing, i.e. the laser beam was hidden from the camera by the surface roughness (Darboux & Huang, 2003). In order to reduce the number of missing points, two records, with a rotation of 180° between them, were taken for each DEM retrieval. The frames were then truncated and the pair of records repositioned by intercorrelation. The data from both pairs were then merged by keeping the data found exclusively on each record and averaging the repetitive data. The remaining 7% of missing data points were estimated by nearest neighbour interpolation. The main absolute difference between the common elevation points of a pair of records was slightly less than 1 mm. So, the vertical precision of the final DEM was 1 mm in our case. Thus, the elevations were re-scaled at 1 mm resolution.

For each DEM, the mean plane estimated by linear regression has been removed and the spatial mean is zero.

$$m_p^{(k)} = \frac{1}{N_p^2} \sum_{i=0}^{N_p-1} \sum_{j=0}^{N_p-1} S_p^{(k)}\left(x_i; y_j\right) = 0 \tag{1}$$

The quantity N_p designates the number of samples along the Ox- or Oy- axis for the pth- soil surface with $N_1 = N_2 = 1000$. The pairs $(x_i; y_j)$ give the coordinates of sampling points with $x_i = i\Delta_p$ and $y_j = j\Delta_p$. The sampling interval Δ_p is equal to 0.5 mm for $p = 1$ and $p = 2$. Fig. 1 shows the laboratory soil surfaces without their mean plane.

2.1.2. Current roughness indices

In results section, we shall consider current roughness indices characterising soil surface roughness and determine the correlations with the parameters of autocorrelation model. The first one is the chain index SCI as defined in Gilliot et al. (2017) as:

$$SCI_p^{(k)} = \left(1 - \frac{1}{SSA_p^{(k)}}\right) \times 100 \tag{2}$$

where SSA is the specific surface area index (Helming, Jeschke, & Storl, 1992) defined as the ratio between the area of the real 3D surface and the projected area on the reference plane. In Helming et al. (1992), SSA was computed by summing up the surface area of all elementary grid squares at surface resolution. It was also related to the slope at each grid square. So that, in Taconet et al. (2010) and Gilliot et al. (2017), SSA was derived from the slope at each DEM voxel. In this paper, we propose to estimate SSA in a different way because it appears to us simpler to use voxel gradients than the angles between the normal and the vertical vectors. SSA is computed by integrating the gradient norm GN of the surface data points $M(x, y, z = S(x, y))$, with $S = S_p^{(k)}$ in this study:

$$GN = \sqrt{1 + \left(\frac{dS}{dx}\right)^2 + \left(\frac{dS}{dy}\right)^2} \tag{3}$$

where $\frac{dS}{dx}$ and $\frac{dS}{dy}$ correspond to the differences in x and y directions. Indeed, this amounts to consider all elementary displacements for point M to point M' with a linear approximation.

Then, the mean weighted diameter of the clods $MWD_p^{(k)}$ is estimated after clod segmentation from the DEMs as in Taconet et al. (2010) or in Vannier et al. (2019),

$$MWD_p^{(k)} = \sum_{i=1}^{n_p^{(k)}} \mathcal{D}_i . s_i \tag{4}$$

where $n_p^{(k)}$ is the total number of clods in surface $S_p^{(k)}$, $\mathcal{D}_i$ is the equivalent diameter of clod i (estimated here from the area of clod, considered as a disc) and s_i is the fraction of the surface area covered by clod i:

$$s_i = \frac{\mathcal{A}_i}{\sum\limits_{j=1}^{n_p^{(k)}} \mathcal{A}_j} \tag{5}$$

Also we consider the volume occupied by the clods as in Vannier et al. (2018a), and report the total volume $TV_p^{(k)}$:

$$TV_p^{(k)} = \sum_{j=1}^{n_p^{(k)}} V_j \tag{6}$$

where V_j is the volume of clod j.

2.2. Model of the bi-dimensional soil surface autocorrelation

2.2.1. Definition and properties of the autocorrelation function

The bi-dimensional autocorrelation function $C_p^{(k)}(x, y)$ of the soil surface $S_p^{(k)}(x, y)$ measures the similarity between the function $S_p^{(k)}(x, y)$ and its shifted (lagged) copy along the
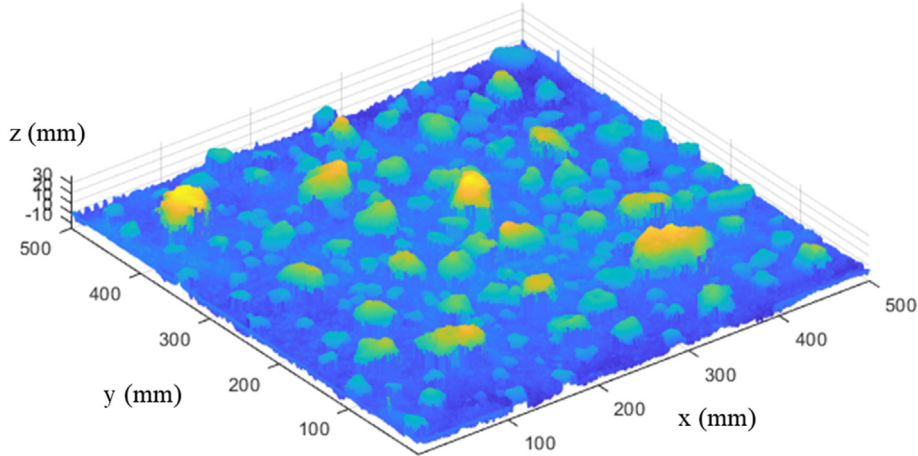
Fig. 2 – 2.5D DEM of second laboratory soil surface with high clod concentration at initial stage.

directions x and y as a function of the two lags. In fact, it describes the degree of spatial dependence of the soil surface function. A biased estimator is used to compute the autocorrelation function $C_p^{(k)}(x, y)$ at the sampling points $(x_i; y_j)$ and the raw autocorrelation (the double summation) is scaled by the total number of samples, i.e. divided by N_p^2. The estimate is unbiased when the raw autocorrelation is divided by the number of samples in the double summation, i.e. divided by $(N_p - |i|) \times (N_p - |j|)$. A biased estimate usually has a smaller mean squared error (Percival & Walden, 1993).

If $0 \leq i \leq N_p - 1$ and $0 \leq j \leq N_p - 1$

$$C_p^{(k)}\left(x_i, y_j\right) = \frac{1}{N_p^2} \sum_{m=0}^{N_p-1-i} \sum_{n=0}^{N_p-1-j} S_p^{(k)}(x_m; y_n) S_p^{(k)}\left(x_{i+m}; y_{j+n}\right) \tag{7a}$$

If $1 - N_p \leq i \leq 0$ and $0 \leq j \leq N_p - 1$

$$C_p^{(k)}\left(x_i, y_j\right) = \frac{1}{N_p^2} \sum_{m=-i}^{N_p-1} \sum_{n=0}^{N_p-1-j} S_p^{(k)}(x_m; y_n) S_p^{(k)}\left(x_{i+m}; y_{j+n}\right) \tag{7b}$$

If $0 \leq i \leq N_p - 1$ and $1 - N_p \leq j \leq 0$

$$C_p^{(k)}\left(x_i, y_j\right) = \frac{1}{N_p^2} \sum_{m=0}^{N_p-1-i} \sum_{n=-j}^{N_p-1} S_p^{(k)}(x_m; y_n) S_p^{(k)}\left(x_{i+m}; y_{j+n}\right) \tag{7c}$$

If $1 - N_p \leq i \leq 0$ and $1 - N_p \leq j \leq 0$

$$C_p^{(k)}\left(x_i, y_j\right) = \frac{1}{N_p^2} \sum_{m=-i}^{N_p-1} \sum_{n=-j}^{N_p-1} S_p^{(k)}(x_m; y_n) S_p^{(k)}\left(x_{i+m}; y_{j+n}\right) \tag{7d}$$

In the other cases, $C_p^{(k)}(x_i, y_j) = 0$. The autocorrelation function $C_p^{(k)}(x, y)$ is estimated at the data points (x_i, y_j) by the MATLAB® command *xcorr*.

Recalling that the autocorrelation function is symmetrical with respect to the origin;

$$\forall x, \ C_p^{(k)}(-x, 0) = C_p^{(k)}(+x, 0)$$
$$\forall y, \ C_p^{(k)}(0, -y) = C_p^{(k)}(0, +y) \tag{8}$$

The autocorrelation function is maximal at the origin and the value $C_p^{(k)}(0, 0)$ corresponds to the second-order spatial moment of $S_p^{(k)}(x, y)$. Because the spatial mean is zero, the second-order moment becomes identified with the variance $V_p^{(k)} = \left(\sigma_p^{(k)}\right)^2$ and the rms-height with the standard deviation of heights and $\sigma_p^{(k)}$ is given by:

$$\sigma_p^{(k)} = \sqrt{C_p^{(k)}(0, 0)} = \sqrt{\frac{1}{N_p^2} \sum_{m=0}^{N_p-1} \sum_{n=0}^{N_p-1} \left(S_p^{(k)}(x_m; y_n)\right)^2} \tag{9}$$

2.2.2. A five-parameter model for the autocorrelation function

It is proposed to represent the autocorrelation function $C_p^{(k)}(x, y)$ by a five-parameter model $\tilde{C}_p^{(k)}(x, y)$ which verifies the symmetry property with respect to the origin:

$$\tilde{C}_p^{(k)}(x, y) = \left(\sigma_p^{(k)}\right)^2 \exp\left(-\left[\left(\frac{X}{l_{p,X}^{(k)}}\right)^2 + \left(\frac{Y}{l_{p,Y}^{(k)}}\right)^2\right]^{r_p^{(k)}}\right) \tag{10}$$

with $X = x\cos(\delta_p^{(k)}) + y\sin(\delta_p^{(k)})$ and $Y = -x\sin(\delta_p^{(k)}) + y\cos(\delta_p^{(k)})$. The rms-height $\sigma_p^{(k)}$ will be estimated by Eq. (9). The quantities $l_{p,X}^{(k)}$ and $l_{p,Y}^{(k)}$ denotes the correlation lengths along the main axes OX and OY. The tilt angle $\delta_p^{(k)}$ is the angle between the axes OX and Ox. The last parameter $r_p^{(k)}$ is the roughness exponent.

If both correlation lengths $l_{p,X}^{(k)}$ and $l_{p,Y}^{(k)}$ are equal, the soil surface is isotropic otherwise it is anisotropic. Adapting the isotropy index used in Dusséaux et al. (2012), we can define $I_p^{(k)}$ as:

$$I_p^{(k)} = \frac{min\left(l_{p,X}^{(k)}; l_{p,Y}^{(k)}\right)}{max\left(l_{p,X}^{(k)}; l_{p,Y}^{(k)}\right)} \tag{11}$$

For an isotropic soil surface, the isotropy index is maximum and equal to 1. The degree of anisotropy $J_p^{(k)}$ of a soil

surface is traduced by a decrease of the isotropy index and can be estimated as:

$$J_p^{(k)} = 1 - I_p^{(k)} \tag{12}$$

When $J_p^{(k)} = 0$ and $r_p^{(k)} = 1$, the autocorrelation function is isotropic and it becomes identified with a Gaussian function. When $J_p^{(k)} = 0$ and $r_p^{(k)} = 0.5$, it becomes identified with a bi-exponential function. The intermediate Gaussian-exponential model given by Eq. (10) is often used in remote sensing but in a version with three parameters (i.e., with the rms-height, the correlation length along an axis and the roughness exponent) reducing the characterisation of soils to 1D profiles (Fung, Li, & Chen, 1992, Li, Shi, & Chen, 2002, Zribi, Ciarletti, Taconet, Paillé, & Boissard, 2000a-b, 2005 and 2014, Zheng et al., 2019) or only applicable for isotropic two-dimensional surfaces (Dusséaux et al., 2012). The previous research papers do not provide access to the correlation lengths along the main axes and to the tilt angle.

2.2.3. Estimation of the correlations lengths and the tilt angle

By definition, the correlation lengths are obtained from the level curve of $C_p^{(k)}(x, y)$ for the value $V_p^{(k)} \exp(-1)$. Applying this definition to the autocorrelation function model $\tilde{C}_p^{(k)}(x, y)$, the equation of a standard ellipse centred at the origin is:

$$\left(\frac{x \cos(\delta_p^{(k)}) + y \sin(\delta_p^{(k)})}{l_{p,X}^{(k)}} \right)^2 + \left(\frac{-x \sin(\delta_p^{(k)}) + y \cos(\delta_p^{(k)})}{l_{p,Y}^{(k)}} \right)^2 = 1 \tag{13}$$

If $l_{p,X}^{(k)} = l_{p,Y}^{(k)}$, the contour plot is a circle expressing the isotropy of the surface. By substituting $y = 0$ (or $x = 0$) into Eq. (10), we obtain the correlation length along the Ox axis (or Oy axis) with:

$$l_{p,x}^{(k)} = \frac{1}{\sqrt{\left(\frac{\cos(\delta_p^{(k)})}{l_{p,X}^{(k)}} \right)^2 + \left(\frac{\sin(\delta_p^{(k)})}{l_{p,Y}^{(k)}} \right)^2}} \tag{14a}$$

$$l_{p,y}^{(k)} = \frac{1}{\sqrt{\left(\frac{\sin(\delta_p^{(k)})}{l_{p,X}^{(k)}} \right)^2 + \left(\frac{\cos(\delta_p^{(k)})}{l_{p,Y}^{(k)}} \right)^2}} \tag{14b}$$

By using the polar coordinates $x = r\cos\theta$ and $= r\sin\theta$, and applying some trigonometric formulas, from Eq. (13) it can be seen that for an ellipse, $\rho(\theta) = \frac{2}{r^2}$ is a periodic function, of period π, the Fourier series expansion of which being:

$$\rho(\theta) = a_{p,0}^{(k)} + a_{p,1}^{(k)} \cos(2\theta) + b_{p,1}^{(k)} \sin(2\theta) \tag{15}$$

with

$$a_{p,0}^{(k)} = \frac{1}{\left(l_{p,X}^{(k)} \right)^2} + \frac{1}{\left(l_{p,Y}^{(k)} \right)^2} \tag{16a}$$

$$a_{p,1}^{(k)} = \left(\frac{1}{\left(l_{p,X}^{(k)} \right)^2} - \frac{1}{\left(l_{p,Y}^{(k)} \right)^2} \right) \cos\left(2\delta_p^{(k)} \right) \tag{16b}$$

$$b_{p,1}^{(k)} = \left(\frac{1}{\left(l_{p,X}^{(k)} \right)^2} - \frac{1}{\left(l_{p,Y}^{(k)} \right)^2} \right) \sin\left(2\delta_p^{(k)} \right) \tag{16c}$$

The tilt angle $\delta_p^{(k)}$ and the two correlation lengths $l_{p,X}^{(k)}$ and $l_{p,Y}^{(k)}$ are deduced from the Fourier coefficients $a_{p,0}^{(k)}$, $a_{p,1}^{(k)}$ and $b_{p,1}^{(k)}$ by the relationships:

$$2\delta_p^{(k)} = \arctan\left(\frac{b_{p,1}^{(k)}}{a_{p,1}^{(k)}} \right) [\pi] \tag{17a}$$

$$l_{p,X}^{(k)} = \sqrt{ \frac{2}{a_{p,0}^{(k)} \pm \sqrt{ \left(a_{p,1}^{(k)} \right)^2 + \left(b_{p,1}^{(k)} \right)^2 }} } \tag{17b}$$

$$l_{p,Y}^{(k)} = \sqrt{ \frac{2}{a_{p,0}^{(k)} \mp \sqrt{ \left(a_{p,1}^{(k)} \right)^2 + \left(b_{p,1}^{(k)} \right)^2 }} } \tag{17c}$$

The determination of the tilt angle and the two correlation lengths is done in three steps. Firstly, the level curve of $C_p^{(k)}(x, y)$ for the value $V_p^{(k)}/e$ is obtained by using the MATLAB® function "contour". The contour plot is made on $M_p^{(k)}$ points whose Cartesian coordinates (x_m, y_m) are known. In the second step, the polar coordinates (r_m, θ_m) of each point are defined and the periodic function $\rho(\theta)$ given by Eq. (15) is obtained and the Fourier coefficients $a_{p,0}^{(k)}$, $a_{p,1}^{(k)}$ and $b_{p,1}^{(k)}$ are computed. In the third step, the tilt angle and the two correlation length are computed from Eq. (17). The solution is non-unique: two tilt angles are possible and two pairs of signs, $(+; -)$ or $(-; +)$, can be assigned for the two correlation lengths. For each possible set of parameters $(l_{p,X}^{(k)}; l_{p,Y}^{(k)}; \delta_p^{(k)})$, the associated ellipse is plotted and the coordinates $(\tilde{r}_m, \theta_m)$ of the points on this ellipse are determined. The three parameters retained as solutions are those which minimise the quadratic error $e_{c,p}^{(k)}$ defined by:

$$e_{c,p}^{(k)} = \frac{1}{M_p^{(k)}} \sum_{m=1}^{M_p^{(k)}} \left| 1 - \frac{\tilde{r}_m}{r_m} \right|^2 \tag{18}$$

2.2.4. Estimation of the roughness exponent

Once the four parameters $(\sigma_p^{(k)}; l_{p,X}^{(k)}; l_{p,Y}^{(k)}; \delta_p^{(k)})$ are determined, the roughness exponent is computed from the level curves of the autocorrelation function $C_p^{(k)}(x, y)$ for the values $V_p^{(k)} \exp(-\tau)$ where τ varies between a minimum τ_m and a maximum τ_M with the increment $\Delta\tau$. These level curves are also obtained by using the MATLAB® function "contour". The level curve of the modelled autocorrelation function $\tilde{C}_p^{(k)}(x, y)$ for the value $V_p^{(k)} \exp(-\tau)$ becomes identified with the ellipse given by:

$$\left(\frac{x\cos(\delta_p^{(k)})+y\sin(\delta_p^{(k)})}{l_{p,X}^{(k)}}\right)^2 + \left(\frac{-x\sin(\delta_p^{(k)})+y\cos(\delta_p^{(k)})}{l_{p,Y}^{(k)}}\right)^2 = \tau^{(1/r_p^{(k)})} \tag{19}$$

Let us $(x(\tau);y(\tau))$ be the Cartesian coordinates of the points on the τ-contour. For $\tau = 1$, we obtain the ellipse given the correlation lengths. Consequently, we find that $x(\tau=1)=l_{p,x}^{(k)}$ and $y(\tau=1)=l_{p,y}^{(k)}$ where the correlation lengths along the Ox and Oy axes are given by Eq. (14a) and Eq. (14b), respectively.

Let us reason on the Ox axis and take $y = 0$. Taking into account the remarks above, we show from Eq. (19) that $r_p^{(k)}$ is the slope of the following linear equation where the symbol ln designates the natural logarithm function:

$$\ln(\tau)=2r_p^{(k)}\,ln\left(\frac{x(\tau)}{l_{p,x}^{(k)}}\right) \tag{20}$$

For each value of τ, the value $x(\tau)$ can be computed from the τ-level curves and the parameter $r_p^{(k)}$ can therefore be determined by linear regression. We can also estimate the roughness exponent by reasoning on the Oy axis, on any axis passing through the origin or on the average distances between the points on the contours and the origin. The parameter $r_p^{(k)}$ is estimated from these average distances $\overline{d}_p^{(k)}(\tau)$.

The τ-level curve of $C_p^{(k)}(x,y)$ is obtained by using the MATLAB® function "*contour*" and the τ-contour plot is made on $M_p^{(k)}(\tau)$ points whose Cartesian coordinates $(x_m(\tau),y_m(\tau))$ are known. The average distance $\overline{d}_p^{(k)}(\tau)$ is defined as follows,

$$\overline{d}_p^{(k)}(\tau)=\frac{1}{M_p^{(k)}(\tau)}\sum_{m=1}^{M_p^{(k)}(\tau)}\sqrt{(x_m(\tau))^2+\left(y_m(\tau)\right)^2} \tag{21}$$

For $\tau = 1$, the average distance $\overline{d}_p^{(k)}(\tau)$ corresponds to the average correlation length $\overline{l}_p^{(k)}$. Finally, a linear regression is made on the pairs $(2\,ln(\overline{d}_p^{(k)}(\tau)\,/\overline{l}_p^{(k)});ln(\tau))$ for many values of τ. The slope of this linear regression gives the roughness exponent estimation and in theory, the y-intercept α must be equal to zero. For each soil surface $S_p^{(k)}$, the mean square error $mse_p^{(k)}$ of the linear regression is given.

2.2.5. Validation of the modelled autocorrelation function

Once the five parameters $(\sigma_p^{(k)};l_{p,X}^{(k)};l_{p,Y}^{(k)};\delta_p^{(k)},r_p^{(k)})$ are determined, the modelled autocorrelation function $\tilde{C}_p^{(k)}(x,y)$ can be plotted and compared with the reference autocorrelation function $C_p^{(k)}(x,y)$ estimated from the DEM. For measuring the proximity between the two curves, we determine the error function $\varepsilon_p^{(k)}(x_i,y_j)$ at each sample point (x_i,y_j):

$$\varepsilon_p^{(k)}\left(x_i,y_j\right)=\frac{C_p^{(k)}\left(x_i,y_j\right)-\tilde{C}_p^{(k)}\left(x_i,y_j\right)}{C_p^{(k)}(0,0)} \tag{22}$$

We estimate the mean error $\overline{\varepsilon}_{xy,p}^{(k)}$ and the standard deviation $\sigma_{xy,p}^{(k)}$ of the error function from the sample points defining the central lobe of autocorrelation function.

In the next section, the level curves of the reference autocorrelation function $C_p^{(k)}(x,y)$ and the modelled one $\tilde{C}_p^{(k)}(x,y)$ for different percentages q of the variance $V_p^{(k)}$ are compared. In addition, using least squares the correlation length and roughness exponent of a three-parameter model of the autocorrelation function are estimated:

$$\tilde{C}_p^{(k)}(x,y)=\left(\sigma_p^{(k)}\right)^2 exp\left(-\left(\frac{x^2+y^2}{l_p^{(k)2}}\right)^{r_p^{(k)}}\right) \tag{23}$$

3. Results

3.1. On the references roughness indices

All the reference roughness indices are shown in Table 2. With an increase followed by decrease, the total volume occupied by the clods, TV, shows that the clods swelled during the first rainfall event and then eroded. The values of TV, as well as MWD, show that clods are generally smaller on the second laboratory soil surface. Since it decreases, the SCI index reflects well the erosion of the surfaces under rainfall impact and captures the increase of rainfall intensity. With clods of different size and closeness, the kinetic of the two surfaces are slightly different. The erosion is faster on the second surface having smaller and closer clods. The MWD index increases due to the disappearance of the smallest clods. It can be seen that the correlation length follows the increase of MWD, with high correlations of 87.2% and 98.8% between the two variables for the first and second surface respectively. The correlation length obtained with the three-parameter model is also highly correlated with SCI, evolving in the opposite direction. Correlation coefficients for both surfaces amount to 97.4% and 98.2% respectively. Both indices show that the initial difference of roughness between the two soil surfaces vanished after five rainfalls. The roughness exponent derived from the

Table 2 − Reference roughness indices.						
State k	0	1	2	3	4	5
$TV_1^{(k)}\times10^6$ mm^3	1.626	1.815	1.750	1.673	1.582	1.414
$TV_2^{(k)}\times10^6$ mm^3	1.254	1.389	1.379	1.272	1.227	1.144
$SCI_1^{(k)}$	25.5	23.6	22.6	19.8	18.0	15.2
$SCI_2^{(k)}$	27.6	24.0	21.3	19.2	16.8	14.9
$MWD_1^{(k)}$ mm	36.6	40.1	41.2	43.6	44.5	45.0
$MWD_2^{(k)}$ mm	27.2	29.7	31.0	31.4	32.4	35.5
$l_1^{(k)}$[a] mm	17.3	17.6	18.3	18.8	19.8	21.3
$l_2^{(k)}$[a] mm	16.0	16.9	17.8	18.4	19.2	20.9
$r_1^{(k)}$[a]	0.69	0.70	0.71	0.72	0.73	0.73
$r_2^{(k)}$[a]	0.68	0.70	0.71	0.72	0.72	0.72
[a] With three-parameter model of the autocorrelation function.						

Table 3 − Surface rms-heights $\sigma_p^{(k)}$ for soil surfaces at initial state and at the states after rainfall events.						
State k	0	1	2	3	4	5
$\sigma_1^{(k)}$ mm	8.6	8.9	8.8	8.2	7.8	7.2
$\sigma_2^{(k)}$ mm	8.5	8.7	8.5	8.1	7.7	7.1

three-parameter model was close for the two surfaces. It increased slightly with cumulative rainfall and reached a plateau. With a mean value of about 0.71, it was between the exponential and the Gaussian autocorrelation function. It evolved from displaying exponential behaviour to a more Gaussian behaviour, which can reflect the smoothing effect of rainfall. The rms-heights is also a reference roughness index, but it is included in the model of the autocorrelation function and is commented on in section 3.2.

3.2. On the root-mean square height

Table 3 shows the values of the rms-height $\sigma_p^{(k)}$ for the twelve plots under study. For a given state of the two laboratory made soil surfaces, the rms-heights are close. The relative variation between the initial and final values of the rms-height is equal to 16.3% for the first surface and to and 16.5% for the second.

The rms-height is highly correlated to the total volume occupied by the clods (in Table 2), with correlation coefficients of 93.6% for the first surface and of 88.8% for the second. If only the decreasing part from the second rainfall is considered, then the correlation coefficients increase up to 98.8% for both surfaces. For this decreasing part, the rms-height is also highly correlated with the SCI roughness index (see Table 2) with correlation coefficients of 99.9% and 97.4% respectively.

3.3. On the correlation lengths and the inclination angle

Table 4 shows the values of the correlation lengths $l_{p,X}^{(k)}$ and $l_{p,Y}^{(k)}$ and the values of the ellipse tilt angle $\delta_p^{(k)}$ for the twelve plots at our disposal. The correlation lengths show an increasing trend. Indeed, an increase of MWD and correlation lengths correlated to MWD were observed. It should be noted that MWD reached a maximum correlation coefficient of 95.5% with the correlation length $l_{1,X}^{(k)}$ for the first soil surface, whereas it was 87.2% with the correlation length of the three-parameter model $l_1^{(k)}$ (and only 66.2% for $l_{1,Y}^{(k)}$ due to initial decrease). For the second soil surface, the maximum of 99.0% was obtained with $l_{2,Y}^{(k)}$ but the correlation lengths of the five-parameter model and of the three-parameter model were correlated at more than 99.8%, so that MWD had also elevated correlation coefficients of 98.8% and 98.3% with $l_2^{(k)}$ and $l_{2,X}^{(k)}$, respectively.

The first laboratory made soil surface in its initial state was quasi-isotropic with an isotropic factor $I_1^{(0)}$ equal to 97%. Under

the cumulative effect of the rainfalls, anisotropy appeared and in the last state, the isotropic factor $I_1^{(5)}$ was equal to 86%, traducing the anisotropy of 14%. The correlation lengths $l_{1,X}^{(k)}$ and $l_{1,Y}^{(k)}$ along the two main axes increased with cumulative precipitations. The tilt angle $\delta_1^{(0)}$ was equal to 118° but since this surface in its initial state was quasi-isotropic, the ellipse was nearly circular and the angle of inclination played a secondary role in the ellipse parametrisation. After the first rainfall, the average value of the tilt angle was 87.3° and the variations around this mean value were small. Because the tilt angle was close to 90° at all states, then $l_{1,y}^{(k)} \approx l_{1,X}^{(k)}$ and $l_{1,x}^{(k)} \approx l_{1,Y}^{(k)}$. This property can be verified by applying Eq. (14). The correlation lengths along the axes Ox and Oy were obtained and it was found that in the initial state $l_{1,x}^{(0)} = 17.3$ mm and $l_{1,y}^{(0)} = 17.5$ mm (in its initial state, the surface was quasi-isotropic) and in the final state, $l_{1,x}^{(5)} = 19.8$ mm and $l_{1,y}^{(5)} = 23.1$ mm. The initial state was the state with the highest tilt angle, which departed a little from 90° so that $l_{1,x}^{(0)} \approx l_{1,Y}^{(0)}$, which values 17.2 mm and $l_{1,y}^{(0)} \approx l_{1,X}^{(0)}$, which values 17.6 mm. At final state, with a tilt angle of 88°, then $l_{1,x}^{(5)} = l_{1,Y}^{(5)}$ and $l_{1,y}^{(5)} = l_{1,X}^{(5)}$. The relative variation between the initial and final values for the Ox-correlation length was equal to 14.5% and equal to 31.3% for the Oy-correlation length. For water runoff, the trays were set at a 5% slope along the Oy-direction. The relative variation with the correlation length was therefore twice as large in slope direction. It can be seen that for this surface, MWD was best correlated with the correlation length along the Oy-direction.

The second soil surface made in the laboratory already showed some anisotropy of 13% in its initial state. Under the cumulative effect of the rainfalls, this anisotropy was reduced and in the final state, it was equal to 9%. The average value of the tilt angle is 11.8° and the variations around this mean value were< 5°. Taking into account the values of the angles, for the second soil surface, $l_{2,x}^{(k)} \approx l_{2,X}^{(k)}$ and $l_{2,y}^{(k)} \approx l_{2,Y}^{(k)}$ for all states. By applying the system of Equation (14), correlation lengths were obtained along the axes Ox and Oy and it was found that in the initial state $l_{2,x}^{(0)} = 17.2$ mm and $l_{2,y}^{(0)} = 15.1$ mm and in the final state, $l_{2,x}^{(5)} = 21.9$ mm and $l_{2,y}^{(5)} = 20.0$ mm. Also, at the initial state, $l_{2,x}^{(0)} \approx l_{2,X}^{(0)}$ (17.3 mm) and $l_{2,y}^{(0)} \approx l_{2,Y}^{(0)}$ (15.0 mm), and at final state $l_{2,x}^{(5)} = l_{2,X}^{(5)}$ (21.9 mm) and $l_{2,y}^{(5)} = l_{2,Y}^{(5)}$ (20.0 mm). The relative variation between the initial and final values for the Ox-correlation length was equal to 27.3% and equal to 32.5% for the Oy-correlation length. The relative variation was slightly more marked in the Oy-direction defining the 5% slope of the tray. It was noted that for this surface, MWD was best correlated with the correlation length along the Oy-direction.

Table 5 shows the values of the quadratic error $e_{c,p}^{(k)}$ between the modelled ellipse and the reference contour obtained from the autocorrelation function for the twelve plots under study. The error was $< 10^{-4}$ for both the laboratory made soil surfaces and this showed that the ellipse modelled by the two

Table 4 – Estimations of correlations lengths $l_{p,X}^{(k)}$ and $l_{p,Y}^{(k)}$ along the main axes OX and OY and tilt angle $\delta_p^{(k)}$ for two soil surfaces at initial state and at the states after rainfall events.

State k	0	1	2	3	4	5
$l_{1,X}^{(k)}$ mm	17.6	19.0	20.6	20.7	22.0	23.1
$l_{1,Y}^{(k)}$ mm	17.2	16.5	16.8	17.4	18.2	19.8
$\delta_1^{(k)}$ degrees	118	88.6	88.6	83.1	88.1	88.0
$l_{2,X}^{(k)}$ mm	17.3	18	18.9	19.5	20.3	21.9
$l_{2,Y}^{(k)}$ mm	15.0	16.0	16.8	17.4	18.2	20.0
$\delta_2^{(k)}$ degrees	10.8	15.1	12.9	10.4	14.9	6.9

Table 5 − Error $e_{c,p}^{(k)}$ between ellipse derived from estimated parameters $l_{p,X}^{(k)}$, $l_{p,Y}^{(k)}$ and $\delta_p^{(k)}$ and level curve of reference correlation function at the value $e^{-1}V_p^{(k)}$ for two soil surfaces at initial state and at the states after rainfall events.

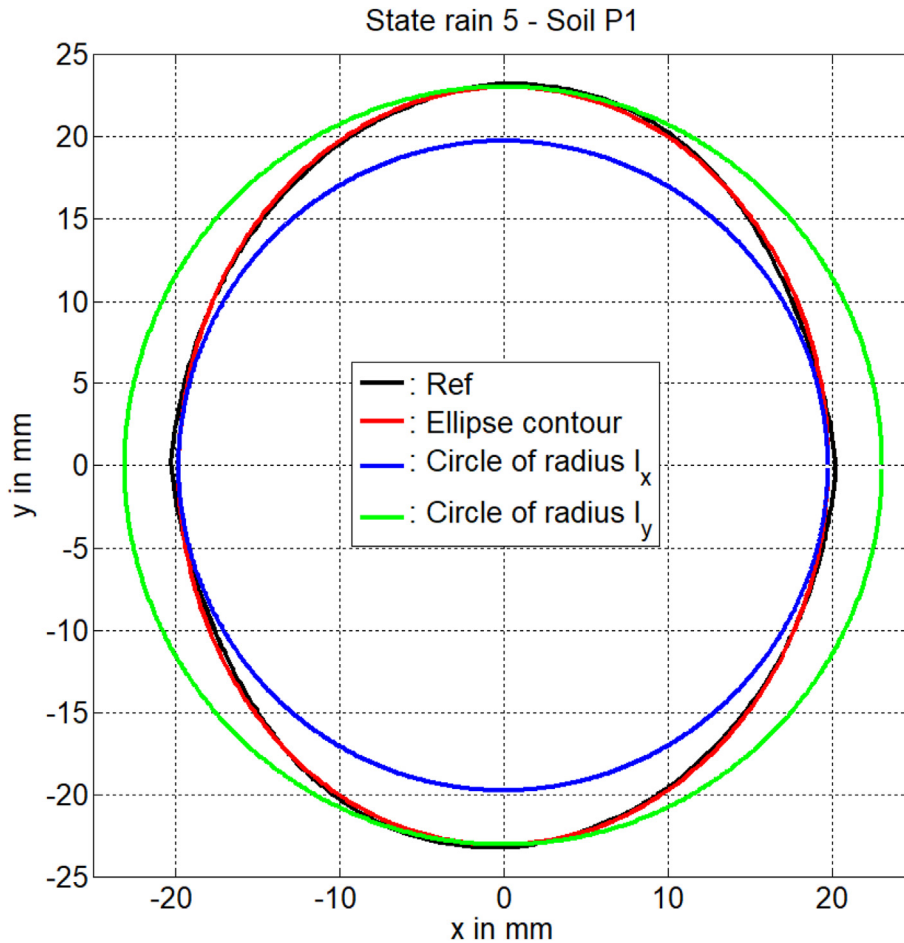| State k	0	1	2	3	4	5
$e_{c,1}^{(k)}$	$2.02 \ 10^{-5}$	$2.35 \ 10^{-5}$	$4.33 \ 10^{-5}$	$6.74 \ 10^{-5}$	$7.51 \ 10^{-5}$	$8.57 \ 10^{-5}$
$e_{c,2}^{(k)}$	$1.03 \ 10^{-5}$	$7.23 \ 10^{-5}$	$6.53 \ 10^{-5}$	$6.08 \ 10^{-5}$	$6.81 \ 10^{-5}$	$8.81 \ 10^{-5}$

Fig. 3 − Level curve of reference autocorrelation function and ellipse or circles passing through correlation lengths for first laboratory soil surface at final state.

correlation lengths and the tilt angle was close to the reference iso-contour providing a correlation lengths in all directions of the plane.

The first laboratory made soil surface in the last state is an anisotropic soil surface with an isotropic factor $I_1^{(5)}$ equal to 86%. Figure 3 shows the reference contour, the modelled ellipse given by Eq. (13) and the circles of radius $l_{1,x}^{(5)}$ and $l_{1,y}^{(5)}$ associated with the soil surface $S_1^{(5)}$. On this horizontal section of the autocorrelation function, the reference contour and the modelled ellipse are superimposed. The reference contour cannot be approached by a circle of radius $l_{1,x}^{(5)}$ or by a circle of radius $l_{1,y}^{(5)}$. Figure 4 also shows a section of the normalised autocorrelation function in the vertical plan, along the directions Ox and Oy. The better fit of the five-parameter model can be seen.

3.4.   On the roughness exponent

Figure 5 shows the data points $(2 \ln(\bar{d}_2^{(0)}(\tau) \ /\bar{l}_2^{(0)}); \ln(\tau))$ for τ varying between $\tau_m = 1/10$ and $\tau_M = 1.2$ with the increment $\Delta\tau = 1/10$. For the second laboratory soil surface ($p = 2$) in the initial state ($k = 0$), the quantity $\bar{l}_2^{(0)}$ designates the average correlation length derived from the level curve of the reference autocorrelation function $C_2^{(0)}(x, y)$ for the value $V_2^{(0)} \exp(-1)$ and the quantity $\bar{d}_2^{(0)}(\tau)$ designates the average distance at the origin for the level curve of $C_2^{(0)}(x, y)$ for the value $V_2^{(0)} \exp(-\tau)$. Figure 5 also shows the linear regression obtained from these data points. The slope of this linear regression gives the roughness exponent $r_2^{(0)}$ equal to 0.67 and
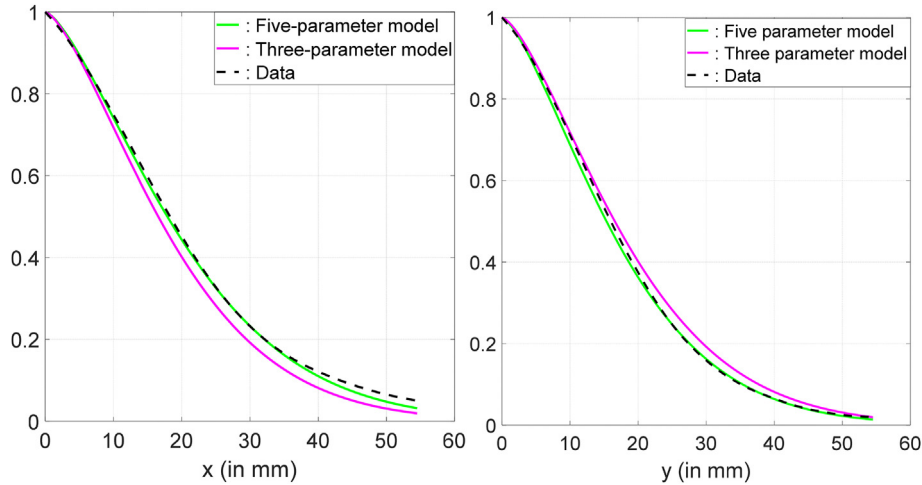
Fig. 4 – Normalised autocorrelation functions with respect to Ox axis (left column) and Oy axis. (right column) for the first laboratory soil surface at final state.
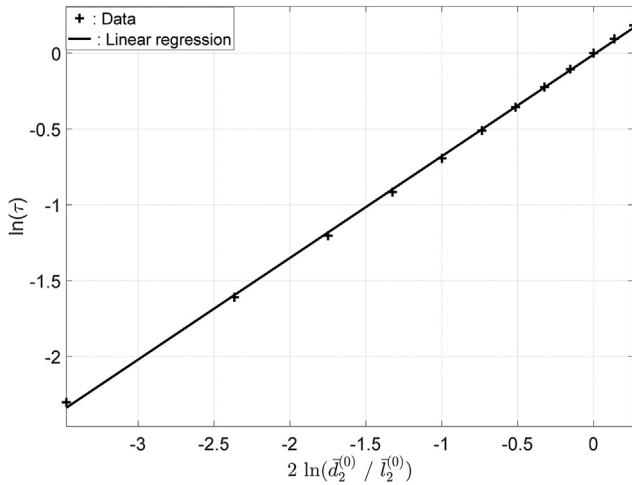

Fig. 5 – Data points $(2\,\ln(\overline{\vec{d}}_2^{(0)}(\tau)\,/\overline{l}_2^{(0)}); \ln(\tau))$ and linear regression for determination of roughness exponent for the second laboratory surface at initial state.

the y-intercept $\alpha_2^{(0)}$ is equal to $-9.2\ 10^{-3}$. The mean square error $mse_2^{(0)}$ of the linear regression is equal to $2.7\ 10^{-4}$. This low value confirms the validity of the linear regression and as shown in Fig. 5, the comparison between the data points and the linear regression line was therefore conclusive.

Table 6 shows the values of the roughness exponent $r_p^{(k)}$ and the y-intercept $\alpha_p^{(k)}$ for the twelve plots at our disposal.

The roughness exponent increases slightly under the effects of successive rainfalls. With such roughness exponent values (ranging between 0.67 and 0.72), the autocorrelation function was neither a bi-exponential nor a Gaussian function but the shape of the curve somewhat in between. For all soil surfaces, the y-intercept value was small and close to the theoretical value of zero. As shown also in Table 6, the mean square errors $mse_p^{(k)}$ were small and this validates the use of estimation of the roughness exponent by linear regression.

It should be noted that the values of roughness exponents obtained with the five-parameter model of the autocorrelation function were very close to those obtained with the three-parameter model (see Table 2).

3.5.   Comparison between the five-parameter model and the reference autocorrelation function

Figure 4 shows an example of reference autocorrelation function along the Ox and Oy direction modelled using the three- and five-parameter models. The five-parameter model showed very good agreement for the main lobe of the reference autocorrelation function along both directions. Figure 6 gives the level curves of the reference autocorrelation function and that modelled for four values of the height expressed as a percentage q of the variance, for three states of the surfaces $S_1^{(k)}$ and $S_2^{(k)}$. The comparisons are conclusive. For $q = 0.8$, 0.6 and e^{-1}, the level curves are superimposed. For $q = 0.2$, there was good agreement. For the second laboratory made

Table 6 – Estimations by linear regression of roughness exponent $r_p^{(k)}$, with y-intercept $\alpha_p^{(k)}$ and mean square error $mse_p^{(k)}$ for soil surfaces at initial state and at the states after rainfall events.

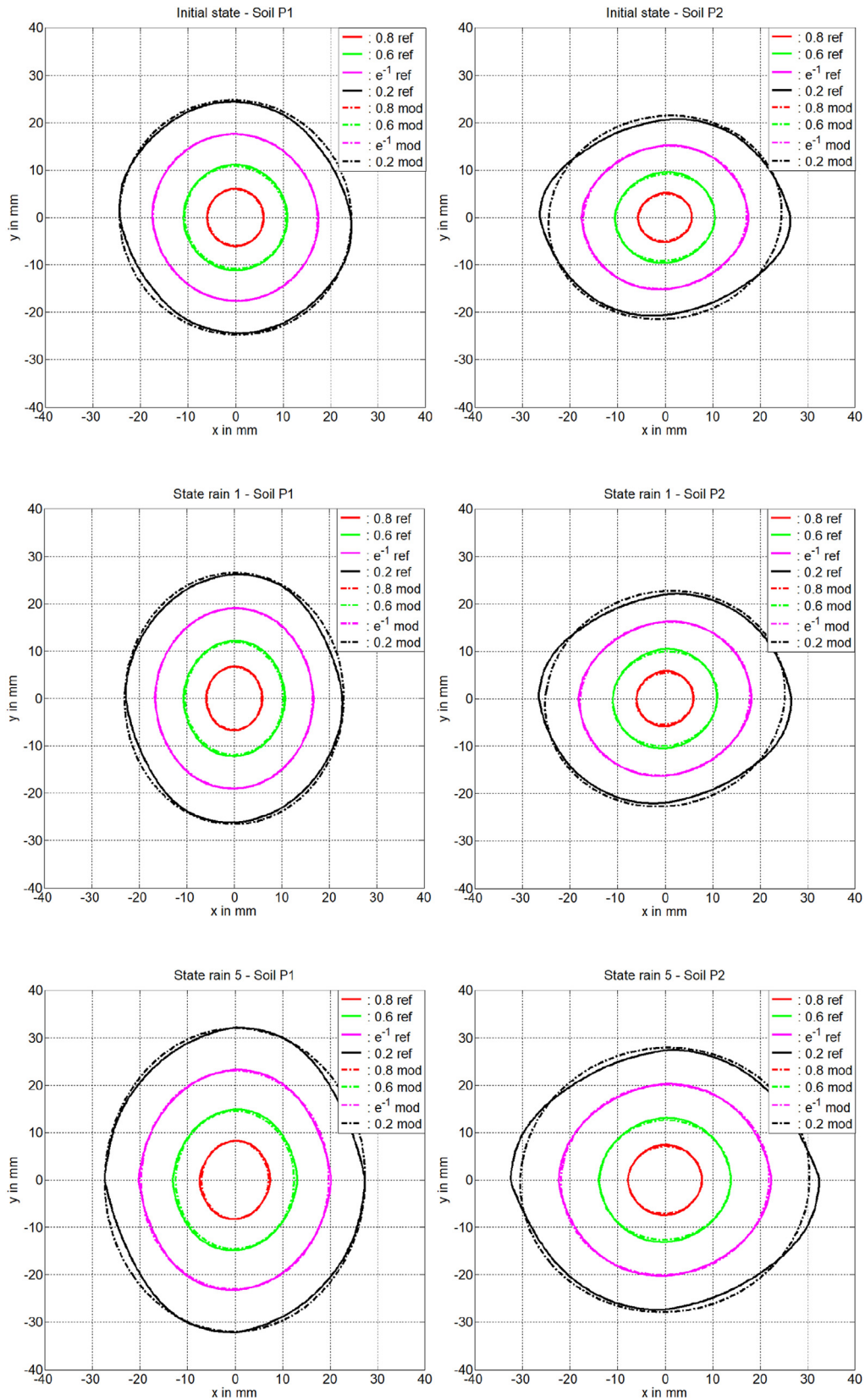| State k	0	1	2	3	4	5
$r_1^{(k)}$	0.68	0.71	0.71	0.72	0.72	0.72
$\alpha_1^{(k)}$	$-1.6\ 10^{-2}$	$-1.6\ 10^{-2}$	$-1.7\ 10^{-2}$	$-1.6\ 10^{-2}$	$-1.6\ 10^{-2}$	$-1.7\ 10^{-2}$
$mse_1^{(k)}$	$7.3\ 10^{-4}$	$7.2\ 10^{-4}$	$7.8\ 10^{-4}$	$7.1\ 10^{-4}$	$6.9\ 10^{-4}$	$7.4\ 10^{-4}$
$r_2^{(k)}$	0.67	0.69	0.70	0.71	0.71	0.72
$\alpha_2^{(k)}$	$-9.2\ 10^{-3}$	$-9.1\ 10^{-3}$	$-7.2\ 10^{-3}$	$-7.6\ 10^{-3}$	$-7.8\ 10^{-3}$	$-8.6\ 10^{-3}$
$mse_2^{(k)}$	$2.7\ 10^{-4}$	$2.3\ 10^{-4}$	$1.3\ 10^{-4}$	$1.6\ 10^{-4}$	$2.0\ 10^{-4}$	$2.0\ 10^{-4}$

Fig. 6 – Level curves of reference autocorrelation function and modelled function for four values of the height expressed as a percentage of the variance. Laboratory made soil surfaces with a low clod concentration (left column), with a high clod concentration (right column).

Table 7 – Mean values $\overline{\varepsilon}_{xy,p}^{(k)}$ of the error function between estimated correlation function and reference correlation function for 3 and five-parameter models.

Model	State k	0	1	2	3	4	5
3 parameter	$\overline{\varepsilon}_{xy,1}^{(k)}$	5.6 10^{-3}	6.6 10^{-3}	6.6 10^{-3}	5.4 10^{-3}	4.0 10^{-3}	2.1 10^{-3}
5 parameter.	$\overline{\varepsilon}_{xy,1}^{(k)}$	4.3 10^{-3}	6.1 10^{-3}	4.0 10^{-3}	3.1 10^{-3}	7.6 10^{-4}	-5.4 10^{-4}
3 parameter	$\overline{\varepsilon}_{xy,2}^{(k)}$	1.9 10^{-3}	1.8 10^{-3}	1.5 10^{-3}	1.5 10^{-3}	2.4 10^{-3}	2.4 10^{-3}
5 parameter	$\overline{\varepsilon}_{xy,2}^{(k)}$	-7.0 10^{-4}	-3.2 10^{-4}	1.0 10^{-4}	-5.0 10^{-4}	1.1 10^{-3}	2.5 10^{-3}

Table 8 – Standard deviations $\sigma_{xy,p}^{(k)}$ of the error function between estimated correlation function and reference correlation function for 3 and five-parameter models.

Model	State k	0	1	2	3	4	5
3 parameter	$\sigma_{xy,1}^{(k)}$	1.57 10^{-2}	2.10 10^{-2}	2.77 10^{-2}	2.57 10^{-2}	2.74 10^{-2}	2.36 10^{-2}
5 parameter	$\sigma_{xy,1}^{(k)}$	1.55 10^{-2}	1.59 10^{-2}	1.75 10^{-2}	1.65 10^{-2}	1.55 10^{-2}	1.37 10^{-2}
3 parameter	$\sigma_{xy,2}^{(k)}$	3.19 10^{-2}	2.70 10^{-2}	2.64 10^{-2}	2.59 10^{-2}	2.63 10^{-2}	2.67 10^{-2}
5 parameter.	$\sigma_{xy,2}^{(k)}$	2.29 10^{-2}	2.03 10^{-2}	1.86 10^{-2}	1.87 10^{-2}	1.92 10^{-2}	2.04 10^{-2}

soil surface, it was seen that there was a difference between the two level curves along the Ox-axis. This difference was due to the flaring of the reference autocorrelation function at the base of its central lobe.

For the two laboratory made surfaces, the area defined by the q-level curve increased with the successive rainfall and the spreading of the clods. For the tray $S_1^{(0)}$, the level curves were almost circular, thus reflecting the isotropy of the surface. Under the cumulative effect of the rainfalls, anisotropy appeared and the level curves stretched along the Oy-axis due to the inclination of the trays in this direction. The second laboratory made soil surface exhibited three states a slight anisotropy. As shown in section 4.2, under the cumulative effect of the rainfall and the inclination of the trays, anisotropy weakly reduced.

Table 7 shows the mean values of the error function (given by Eq. (22)) and estimated from the sample points defining the central lobe of autocorrelation function. Table 8 shows the standard deviations for all the surfaces at our disposal. The mean errors were <1% for all the soil surfaces under consideration and across the whole directions defining the central lobes on average were 0.3% (absolute). The standard deviations were <3.2% for all the soil surfaces under consideration and were on average 1.8% across all directions. These errors defining the proximity between the modelled and reference autocorrelation functions were weak, which illustrates the reliability of the proposed model.

4. Discussion

The bidirectional autocorrelation function used in remote sensing studies is usually modelled by a function of three parameters, rms-height, a single correlation length, and a roughness exponent. This function is thus supposed isotropic. The proposed model of the autocorrelation function developed here has five parameters in order to take into account the anisotropy of soil surfaces and to align the coordinate system into the direction of the maximum correlation length. This led to an accurate fit of the autocorrelation function estimated from DEM which was better than that obtained with a three-parameter model. As shown in Table 7, except in the last state of the second laboratory soil surface, all the mean errors were smaller for the five-parameter model than for the three-parameter model and all the standard deviations of errors were smaller with the five-parameter model than with the three-parameter model. This shows numerically the improvement brought by the proposed model with five-parameters.

The goodness of fit of the autocorrelation function and the relevance of the parameters offered a good description of soil surface roughness. This offers the possibility of modelling taking into account the anisotropy of soil surface. Figure 3 shows that a three-parameter model is ineffective for anisotropic surfaces and does not provide the reference iso-contour giving the correlation lengths in any direction of the plane. It has been shown that the proposed approach is feasible to characterise soil surface roughness with moderate anisotropy under controlled conditions. Future work will consider more strongly anisotropic soil surfaces. It will be necessary to register DEMs larger than 500 × 500 mm in order to highlight the strong anisotropic factors and directional structures that occur due to the furrows. The limitation of 500 mm is due to the used laser scanner used here. Some other photogrammetry methods or another laser scanner will be needed.

The evolution of model parameters under the rain impact requires discussion. The rms-heights and even more the correlation lengths are sensitive to roughness change induced by rainfall. During the first rainfall, an increase of the rms-height could be seen which reflects clod swelling phenomenon as shown in Vannier et al. (2018b). After the second rainfall ($k \geq 2$), as shown in Table 3, the rms-height decreased with cumulative precipitation. This decrease could be related to the erosion of clods by rainfall impact, which causes some levelling of larger clods and the disappearance of smaller ones (Vannier et al., 2018b). Secondly, with the low clod concentration tray, as well as the tray with a high concentration, correlation lengths show an increasing trend (see Table 4).

This increase is related to the spreading of clods under rainfall impact, which was studied by Vannier et al. (2018b). The low clod concentration soil surface in the initial state is quasi-isotropic with an isotropic factor $I_1^{(0)}$ equal to 97%. The high clod concentration soil, in the initial state, had anisotropy of 13% with a correlation length along the Ox axis greater than that along the Oy axis. For water runoff, the trays were set at a 5% slope along the Oy-direction. This slope contributed to a clod stretching along the Oy-direction and this caused anisotropy for the soil surface with a low concentration of clods under the succession of rainfalls. For the second tray, with high clod concentration, the slope of 5% contributed to reduced initial anisotropy that was oriented along the Ox direction. The improvement brought about by a second correlation length was highlighted. The rms-height and both correlation lengths were highly correlated with other roughness indices of reference and they were complementary. They had the advantage to be gathered in a modelling function.

The roughness exponent shows a small increase which was in the direction from exponential to Gaussian behaviour due to the degradation of small clods as explained in Zribi, Baghdadi, Holah, Fafin, and Guérin (2005) in the case of real agricultural soils. The roughness exponents estimated with five- or three-parameter models were very close together and were usually related to soil surface texture. It would be interesting to include higher roughness surfaces to better study this parameter.

This work was conducted with laboratory made soil surfaces approaching seedbeds. Therefore, the parameters were smaller than that of real (field-based) seedbeds. However, there is no obstacle to estimate the five-parameter model from experimental autocorrelation functions of seedbeds recorded in the fields. Flat horizontal supports for the clods occurred, so that the DEMs were centred by subtracting the mean height. With DEMs for natural seedbeds, this step can be carried out by estimating the determined component by either averaging along one direction or extracting first singular values of the DEM (that is a matrix), and then considering the residue representing random roughness.

5. Conclusion

An efficient parametrisation of soil surface roughness was introduced that relies on modelling the bidirectional autocorrelation function estimated from 2.5D DEMs of soil surfaces. The proposed method estimated each parameter of the model and showed robust parameter estimation for two soil surfaces made in the laboratory that were subjected to rainfall.

By introducing a second correlation length, it was possible to capture the evolution of a surface from isotropy to anisotropy or from anisotropy to isotropy under rainfall. The five parameters of the model could be related to surface characteristics.

The goodness of fit of the autocorrelation function and the relevance of the parameters showed feasibility and interest of the method. It opens perspectives for further modelling in remote sensing and geosciences.

Our medium-term goal will be to use this model to describe real agricultural soils (seedbeds soils and soils with more marked tillage). The surface of agricultural soils presents several levels of roughness: that is roughness due to the distribution of clods, due to furrows and that linked to the natural morphology of the soil. Each of these roughness can be characterised by an autocorrelation function. The five-parameter model used to describe the roughness linked to the distribution of clods requires confirmation on real soils. The furrows can be modelled by a random periodic function and the associated autocorrelation function shows oscillations related to the periodicity (Mattia, 2011). Roughness due to the macroforms of the terrain (of the order of several metres) defines the topography of the landscape and the local mean plane on which the other levels of roughness are arranged (Martinez-Agirre et al., 2016). The concept is to in the future define the overall autocorrelation function associated to these three levels of roughness.

Declaration of competing interest

The authors declare that they have no known competing financial interests or personal relationships that could have appeared to influence the work reported in this paper.

REFERENCES

Aguilar, M. A., Aguilar, F. J., & Negreiros, J. (2009). Off-the-shelf laser scanning and close-range digital photogrammetry for measuring agricultural soils microrelief. *Biosystems Engineering, 103*, 504–517. https://doi.org/10.1016/j.biosystemseng.2009.02.010

Anderson, K., & Kuhn, N. J. (2008). Variations in soil structure and reflectance during a controlled crusting experiment. *International Journal of Remote Sensing, 29*, 3457–3475. https://doi.org/10.1080/01431160701767435

Atkinson, P. M., & Lewis, P. (2000). Geostatistical classification for remote sensing: An introduction. *Computers & Geosciences, 26*, 361–371. https://doi.org/10.1016/S0098-3004(99)00117-X

Azizi, A., Abbaspour-Gilandeh, Y., Vannier, E., Dusséaux, R., Mseri-Gundoshmian, T., & Moghaddam, H. A. (2020). Semantic segmentation: A modern approach for identifying soil clods in precision farming. *Biosystems Engineering, 196*, 172–182. https://doi.org/10.1016/j.biosystemseng.2020.05.022

Balaguer, A., Ruiz, L. A., Hermosilla, T., & Recio, J. A. (2010). Definition of a comprehensive set of texture semi-variogram features and their evaluation for object-oriented image classification. *Computers & Geosciences, 36*, 231–240. https://doi.org/10.1016/J.CAGEO.2009.05.003

Blaes, X., & Defourny, P. (2008). Characterizing bidimensional roughness of agricultural soil surfaces for SAR modeling. *IEEE Transactions on Geoscience and Remote Sensing, 46*, 4050–4061. https://doi.org/10.1109/TGRS.2008.2002769

Bullard, J. E., Ockelford, A., Strong, C. L., & Aubault, H. (2018). Impact of multi-day rainfall events on surface roughness and physical crusting of very fine soils. *Geoderma, 313*, 181–192. https://doi.org/10.1016/j.geoderma.2017.10.038

Burrough, P. A., McDonnel, R. A., & Lloyd, C. D. (1998). *Principles of geographic information systems.* Oxford University Press. Corpus ID: 8407336.

Cerdan, O., Souchère, V., Lecomte, V., Couturier, A., & Le Bissonnais, Y. (2002). Incorporating soil surface crusting processes in an expert runoff model: Sealing and transfer by runoff and erosion related to agricultural management. *Catena, 46*, 189–205. https://doi.org/10.1016/S0341-8162(01)00166-7

Chimi-Chiadjeu, O., Le Hégarat-Mascle, S., Vannier, E., Taconet, O., & Dusséaux, R. (2014). Automatic clod detection and boundary estimation from Digital Elevation Model images using different approaches. *Catena, 118*, 73–83. https://doi.org/10.1016/J.CATENA.2014.02.003

Chimi-Chiadjeu, O., Vannier, E., Dusséaux, R., Le Hégarat-Mascle, S., & Taconet, O. (2013a). Using simulated annealing algorithm to move clod boundaries on seedbed digital elevation model. *Computers & Geosciences, 57*, 68–76. https://doi.org/10.1016/j.cageo.2013.04.009

Chimi-Chiadjeu, O., Vannier, E., Dusséaux, R., & Taconet, O. (2013b). *Soil surface roughness modeling: Limit of global characterization in remote sensing* (pp. 23–26). Dresden, Germany: SPIE remote sensing. https://doi.org/10.1117/12.2028861. September 2013.

Croft, H., Anderson, K., Brazier, R. E., & Kuhn, N. J. (2013). Modeling fine-scale surface structure using geostatistics. *Water Resources Research, 49*, 1858–1870. https://doi.org/10.1002/wrcr.20172

Dalla Rosa, J., Cooper, M., Darboux, F., & Medeiros, J. C. (2012). Soil roughness evolution in different tillage systems under simulated rainfall using a semivariogram-based index. *Soil and Tillage Research, 124*, 226–232. https://doi.org/10.1016/J.STILL.2012.06.001

Darboux, F., Davy, P., Gascuel-Odoux, C., & Huang, C. (2002). Evolution of soil surface roughness and flowpath connectivity in overland flow experiments. *Catena, 46*, 125–139. https://doi.org/10.1002/ESP.313

Darboux, F., & Huang, C.-H. (2003). An instantaneous-profile laser scanner to measure soil surface microtopography. *Soil Science Society of America Journal, 67*, 92–97. https://doi.org/10.2136/sssaj2003.9200

De Keyser, E., Vernieuwe, H., Lievens, H., Álvarez-Mozos, J., De Baets, B., & Verhoest, N. E. C. (2012). Assessment of SAR-retrieved soil moisture uncertainty on modeled soil surface roughness. *International Journal of Applied Earth Observation and Geoinformation, 18*, 176–182. https://doi.org/10.1016/j.jag.2012.01.017

De Oro, L. A., & Buschiazzo, D. E. (2011). Degradation of the soil surface roughness by rainfall in two loess soils. *Geoderma, 164*, 46–53. https://doi.org/10.1016/J.GEODERMA.2011.05.009

Djedouani, N., Afifi, S., & Dusséaux, R. (2021). Inversion of electrical and geometrical parameters of a stratified medium from data derived from the Small Perturbation Method and the Small Slope Approximation. *Progress In Electromagnetics Research B, 94*, 19–36. https://doi.org/10.2528/PIERB21071305

Dusséaux, R., Vannier, E., Taconet, O., & Granet, G. (2012). Study of backscatter signature for seedbed surface evolution under rainfall – influence of radar precision. *Progress in Electromagnetics Research, 125*, 415–437. https://doi.org/10.2528/PIER11102807

Foster, G. R., Eppert, F. P., & Meyer, L. D. (1979). A programmable rainfall simulator for field plots. In *Proceedings of the rainfall simulator workshop.* Oakland, CA: United States Department of Agriculture - Science and Education Administration. Tucson, Arizona. March 7–9, 1979, 45–59, Sidney, Montana.

Agricultural Reviews and Manuals, ARMW-10 https://archive.org/details/CAT80734631/page/44/mode/2up.

Franceschetti, G., & Riccio, D. (2007). *Scattering, natural surfaces and fractals.* Elsevier. https://doi.org/10.1016/B978-0-12-265655-2.X5000-4

Friedrich, H., Melville, B. W., Coleman, S. E., Clunie, T. M., Nikora, V. I., & Goring, D. G. (2006). Three-dimensional properties of laboratory sand waves obtained from two-dimensional autocorrelation analysis. In *Int. Conf. On fluvial hydraulics, river flow 2006* (pp. 1013–1022). https://doi.org/10.1201/9781439833865.ch107. Lisbon, Portugal, 6-8 September 2006.

Fung, A. K., Li, Z., & Chen, K. S. (1992). Backscattering from randomly rough dielectric surface. *IEEE Transactions on Geoscience and Remote Sensing, 30*(2), 356–369. https://doi.org/10.1109/36.134085

Garcia Moreno, R., Diaz Alvarez, M. C., Saa Requejo, A., Valencia Delfa, J. L., & Tarquis, A. M. (2010). Multiscaling analysis of soil roughness variability. *Geoderma, 160*, 22–30. https://doi.org/10.1016/j.geoderma.2010.04.011

Ghorbanian, A., Sahebi, M. R., & Mohammadzadeh, A. (2019). Optimization approach to retrieve soil surface parameters from single-acquisition single-configuration SAR data. *Comptes Rendus Geoscience, 351*, 332–339. https://doi.org/10.1016/j.crte.2018.11.005

Gilliot, J. M., Vaudour, E., & Michelin, J. (2017). Soil surface roughness measurement: A new fully automatic photogrammetric approach applied to agricultural bare fields. *Computers and Electronics in Agriculture, 134*, 63–78. https://doi.org/10.1016/j.compag.2017.01.010

Grohmann, C. H., Smith, M., & Riccomini, C. (2011). Multiscale analysis of topographic surface roughness in the Midland Valley, Scotland. *IEEE Transactions on Geoscience and Remote Sensing, 49*, 1200–1213. https://doi.org/10.1109/TGRS.2010.2053546

Haubrock, S. N., Kuhnert, M., Chabrillat, S., Güntner, A., & Kaufmann, H. (2009). Spatiotemporal variations of soil surface roughness from in-situ laser scanning. *Catena, 79*, 128–139. https://doi.org/10.1016/J.CATENA.2009.06.005

Helming, K., Jeschke, W., & Storl, J. (1992). Surface reconstruction and change detection for agricultural purposes by close range photogrammetry. In W. Fritz, & J. R. Lucas (Eds.), *International archives for photogrammetry and remote sensing, vol. 29. Part. B5. International congress for photogrammetry and remote sensing* (pp. 610–617). Washington, DC: Proceedings of the 17th ISPRS. https://www.isprs.org/proceedings/XXIX/congress/part5/610_XXIX-part5.pdf

Helming, K., Römkens, M. J. M., & Prasad, S. N. (1998). Surface roughness related processes of runoff and soil loss: A flume study. *Soil Science Society of America Journal, 62*(1), 243–250. https://doi.org/10.2136/sssaj1998.03615995006200010031x

Hemmat, A., Ahmadi, I., & Masoumi, A. (2007). Water infiltration and clod size distribution as influenced by ploughshare type, soil water content and ploughing depth. *Biosystems Engineering, 97*, 257–266. https://doi.org/10.1016/J.BIOSYSTEMSENG.2007.02.010

Huang, C., & Bradford, J. M. (1992). Applications of a laser scanner to quantify soil microtopography. *Soil Science Society of America Journal, 56*, 14–21. https://doi.org/10.2136/SSSAJ1992.03615995005600010002X

Kamphorst, E. C., Jetten, V., Guérif, J., Pitkänen, J., Iversen, B. V., Douglas, J. T., et al. (2000). Predicting depressional storage from soil surface roughness. *Soil Science Society of America Journal, 64*, 1749–1758. https://doi.org/10.2136/SSSAJ2000.6451749X

Li, Q., Shi, J., & Chen, K. S. (2002). A generalized power law spectrum and its applications to the backscattering of soil surfaces based on the integral equation model. *IEEE*

Transactions on Geoscience and Remote Sensing, 40, 271—280. https://doi.org/10.1109/36.992784

Martinez-Agirre, A., Alvarez-Mozos, J., & Gimenez, R. (2016). Evaluation of surface roughness parameters in agricultural soils with different tillage conditions using a laser profile meter. *Soil and Tillage Research, 161,* 19—30. https://doi.org/10.1016/J.STILL.2016.02.013

Mattia, F. (2011). Coherent and incoherent scattering from tilled soil surfaces. *Waves in Random and Complex Media, 21,* 278—300. https://doi.org/10.1080/17455030.2011.552533

Moradizadeh, M., & Saradjian, M. R. (2016). The effect of roughness in simultaneously retrieval of land surface parameters. *Physics and Chemistry of the Earth, 94,* 127—135. https://doi.org/10.1016/J.PCE.2016.03.006

Ogilvy, J. A. (1991). *Theory of wave scattering from random rough surfaces.* Bristol: Adam Hilger. https://doi.org/10.1088/0034-4885/50/12/001

Percival, D. B., & Walden, A. T. (1993). *Spectral analysis for physical applications: Multitaper and conventional univariate techniques.* Cambridge University Press. https://doi.org/10.1017/CBO9780511622762

Smith, M. W. (2014). Roughness in the earth sciences. *Earth Science Revue, 136,* 202—225. https://doi.org/10.1016/j.earscirev.2014.05.016

Taconet, O., & Ciarletti, V. (2007). Estimating soil roughness indices on a ridge-and-furrow surface using stereo photogrammetry. *Soil and Tillage Research, 93,* 64—76. https://doi.org/10.1016/j.still.2006.03.018

Taconet, O., Vannier, E., & Le Hégarat-Mascle, S. (2010). A boundary-based approach for clods identification and characterization on a soil surface. *Soil and Tillage Research, 109,* 123—132. https://doi.org/10.1016/j.still.2010.05.006

Trevisani, S., Cavalli, M., & Marchi, L. (2009). Variogram maps form LiDAR data as fingerprints of surface morphology on scree slopes. *Natural Hazards and Earth System Sciences, 9,* 129—133. https://doi.org/10.5194/nhess-9-129-2009

Trevisani, S., Cavalli, M., & Marchi, L. (2012). Surface texture analysis of a high-resoultion DTM: Interpretating an alpine basin. *Geomorphology, 161—162,* 26—39. https://doi.org/10.1016/J.GEOMORPH.2012.03.031

Trevisani, S., & Rocca, M. (2015). Mad: Robust image texture analysis for applications in high resolution geomorphology. *Computers & Geosciences, 81,* 78—92. https://doi.org/10.1016/J.CAGEO.2015.04.003

Vannier, E., Ciarletti, V., & Darboux, F. (2009). Wavelet-based detection of clods on a soil surface. *Computers & Geosciences, 35,* 2259—2267. https://doi.org/10.1016/j.cageo.2009.03.007

Vannier, E., Ciarletti, V., & Gademer, A. (2006). In *A new approach for roughness analysis of soil surfaces.* https://doi.org/10.5281/ZENODO.53468. EUSIPCO, Florence, Italie, 4-8 September, 2006.

Vannier, E., Dusséaux, R., Taconet, O., & Darboux, F. (2019). Wavelet-based clod segmentation on digital elevation models of a soil surface with or without furrows. *Geoderma, 356,* 113933. https://doi.org/10.1016/j.geoderma.2019.113933

Vannier, E., Taconet, O., Dusséaux, R., & Chimi-Chiadjeu, O. (2014). Statistical characterization of bare soil surface microrelief. In M. Marghany (Ed.), *Advance geoscience remote sensing* (pp. 207—228). Rijeka, Croatia: Edition Intech. https://doi.org/10.5772/57244.

Vannier, E., Taconet, O., Dusséaux, R., & Darboux, F. (2018a). A study of clod evolution in simulated rain on the basis of digital elevation models. *Catena, 160,* 212—221. https://doi.org/10.1016/j.catena.2017.09.017

Vannier, E., Taconet, O., Dusséaux, R., & Darboux, F. (2018b). Using digital elevation models and image processing to follow clod evolution under rainfall. *Journal of toxicology and ecology, 2,* 113. https://www.omicsonline.org/open-access/using-digital-elevation-models-and-image-processing-to-follow-clod-evolution-under-rainfall.pdf.

Verhoest, N. E. C.1, Lievens, H., Wagner, W., Álvarez-Mozos, J., Susan Moran, M., & Mattia, F. (2008). On the soil roughness parameterization problem in soil moisture retrieval of bare surfaces from synthetic aperture radar. *Sensors, 8,* 4213—4248. https://doi.org/10.3390/s8074213

Vidal Vázquez, E., Rosa Vieira, S., Clerici De Maria, I., & Paz Gonzàlez, A. (2009). Geostatistical analysis of microrelief of an oxisol as a function of tillage and cumulative rainfall. *Scientia Agricola, 66(2),* 225—232. https://doi.org/10.1590/S0103-90162009000200012

Vinci, A., Todisco, F., Vergni, L., & Torri, D. (2020). A comparative evaluation of random roughness indices by rainfall simulator and photogrammetry. *Catena, 188,* 104468. https://doi.org/10.1016/j.catena.2020.104468

Woodcock, C. E., Strahler, A. H., & Jupp, D. L. B. (1988). The use of variograms in remote sensing: II. Real digital images. *Remote Sensing of Environment, 25,* 349—379. https://doi.org/10.1016/0034-4257(88)90109-5

Zheng, X., Li, L., Chen, S., Jiang, T., Li, X., & Zhao, K. (2019). Temporal evolution characteristics and prediction methods of spatial correlation function shape of rough soil surfaces. *Soil and Tillage Research, 195,* 104417. https://doi.org/10.1016/j.still.2019.104417

Zhixiong, L., Nan, C., Perdrok, U. D., & Hoogmoed, W. B. (2005). Characterisation of soil profile roughness. *Biosystems Engineering, 91,* 369—377. https://doi.org/10.1016/j.biosystemseng.2005.04.004

Zribi, M., Baghdadi, N., Holah, N., Fafin, O., & Guérin, C. (2005). Evaluation of a rough soil surface description with ASAR-Envisat Radar data. *Remote Sensing of Environment, 95,* 67—76. https://doi.org/10.1016/J.RSE.2004.11.014

Zribi, M., Ciarletti, V., & Taconet, O. (2000b). Validation of a rough surface model based on fractional Brownian geometry with SIRC and ERASME Radar data over Orgeval. *Remote Sensing of Environment, 73,* 65—72. https://doi.org/10.1016/S0034-4257(00)00082-1

Zribi, M., Ciarletti, V., Taconet, O., Paillé, J., & Boissard, J. (2000a). Characterisation of the soil structure and microwave backscattering based on numerical three-dimensional surface representation: Analysis with a fractional brownian model. *Remote Sensing of Environment, 72,* 159—169. https://doi.org/10.1016/S0034-4257(99)00097-8

Zribi, M., Gorrab, A., & Baghdadi, N. (2014). A new soil roughness parameter for the modelling of radar backscattering over bare soil. *Remote Sensing of Environment, 152,* 62—73. https://doi.org/10.1016/J.RSE.2014.05.009